Letter | Editors' Suggestion | Featured in Physics

Collective dynamics of natural killer cells interacting with cancer and fibroblast cells

Yun-Xuan Zhang [1,*] Shu-Chen Liu [2] and Lin I [1,†]

[1]*Department of Physics and Center for Complex Systems, National Central University, Jhongli 32001, Taiwan*

[2]*Department of Biomedical Sciences and Engineering, National Central University, Jhongli 32001, Taiwan*

(Received 13 October 2025; accepted 9 April 2026; published 4 June 2026)

Natural killer cells (NKCs) can distinguish the difference between normal and abnormal cells, and kill the latter. Nevertheless, regardless of the past intensive studies on the intracellular crosstalk via extracellular vesicles, the generic dynamical behaviors of the NKCs around its co-cultured cells in their attacking process remains an elusive intriguing issue. Here, using the binary mixtures of NKCs and normal fibroblast/cancer cells, we experimentally reveal the above unexplored issue. It is found that, NKCs initially assess and identify the type of co-cultured cells. For cancer cells, NKCs attach to them, recruit neighboring NKCs to form clusters, and exhibit anchored fluctuating motion around the cancer cells in the killing process, until the death of cancer cells. In response, CCs also aggregate into larger clusters than those of the NKC free case, until their death, to avoid NKC attacking. In contrast, when interacting with normal fibroblasts, NKCs continuously scout around the cells, without forming large clusters. They cause little effect on fibroblast motion.

DOI: 10.1103/mf3s-pcwt

Dynamically, cells belong to the general category of coupled active systems such as flocking birds [1], fish schools [2], and dense bacteria [3–6]. Through different types of mutual coupling, the self-propelled single-cell motion can be affected by neighboring cells. The unfrozen proliferation further enriches the structural and dynamical behaviors. Past studies have demonstrated concerted motions in the forms of multiscale jets, swirls, turbulence, follow-the-leader streaming, and string-type collective migration [1–20]. Those motions could affect structural evolution, and in turn provide feedbacks to affect mutual coupling and collective motion. Examples include the abnormal diffusive cell motion, formation of multiscale cell clusters with fluctuating boundaries, crowding-induced glass transition and two-stage percolating transitions of densifying cell monolayers, topological defect formation, etc. [9,17–22]. They also play important roles in many biological processes such as embryogenesis [23], wound healing [24,25], tumorigenesis [26], and cancer metastasis [27–29].

In addition to previous studies of collective cell dynamics predominantly focused on monotype cells, the dynamical behaviors can be enriched in binary cell mixtures. For example, recent numerical works showed that tuning cell-cell coupling and motility can affect cell aggregation and cell motion [30–32]. Another recent experimental study demonstrated that the slowed-down turbulentlike endothelial motion due to proliferation-induced jamming can be rejuvenated by the clustering enhanced turbulentlike motion of more mobile and more loosely coupled cancer cells [33]. Fractal-like cancer cell cluster boundaries in the densifying cancer-endothelial cell binary mixture were also found [21].

Nevertheless, the dynamical behaviors of immune cells encountering and interacting with abnormal cells remains mostly unexplored from the perspectives of not only immune oncology but also the physics of coupled active systems. In this work, we experimentally address the above issue in the dilute binary mixture of natural killer cells (NKCs) and cancer cells (CCs) on a collagen-coated substrate. The dynamics of binary mixture of NKCs with normal cells, fibroblast cells (FCs), in which NKCs have minimal cytotoxic effect to FCs observed by time lapse, is also investigated as a reference.

NKC is a type of immune cell that plays a crucial role in the innate immune system. It is known for its ability to recognize and destroy infected or abnormal cells, including virus-infected cells and certain cancer cells. Unlike other immune cells such as T or B cells, NKCs do not require prior exposure to a specific pathogen or antigen to become activated [34–40]. Previous studies showed that NKCs distinguish between normal and abnormal cells by recognizing changes in surface proteins such as MHC class I molecules [41,42]. When an NKC identifies a target cell as an abnormal cell, it releases toxic substances to induce apoptosis in the target cell. This rapid response is essential for controlling the early stages of viral infections and preventing the development of some types of tumors. However, little attention has been paid to the intercellular dynamical behaviors of NKCs in the normal and abnormal cell environments.

Here, we use NK-92, primary oral cancer cells, and primary human fibroblasts as NKCs, CCs, and FCs, respectively. Primary oral cancer cells and adjacent normal fibroblasts were isolated in a previous study [43]. For the NKC only experiment (run I), 10^6 NKCs are randomly distributed in a culture dish (3.5 cm diameter). For the CC only experiment (run II), 5×10^4 CCs are randomly distributed in a culture dish. For the

*Contact author: yunxuanzhang1998@gmail.com
†Contact author: lini@phy.ncu.edu.tw

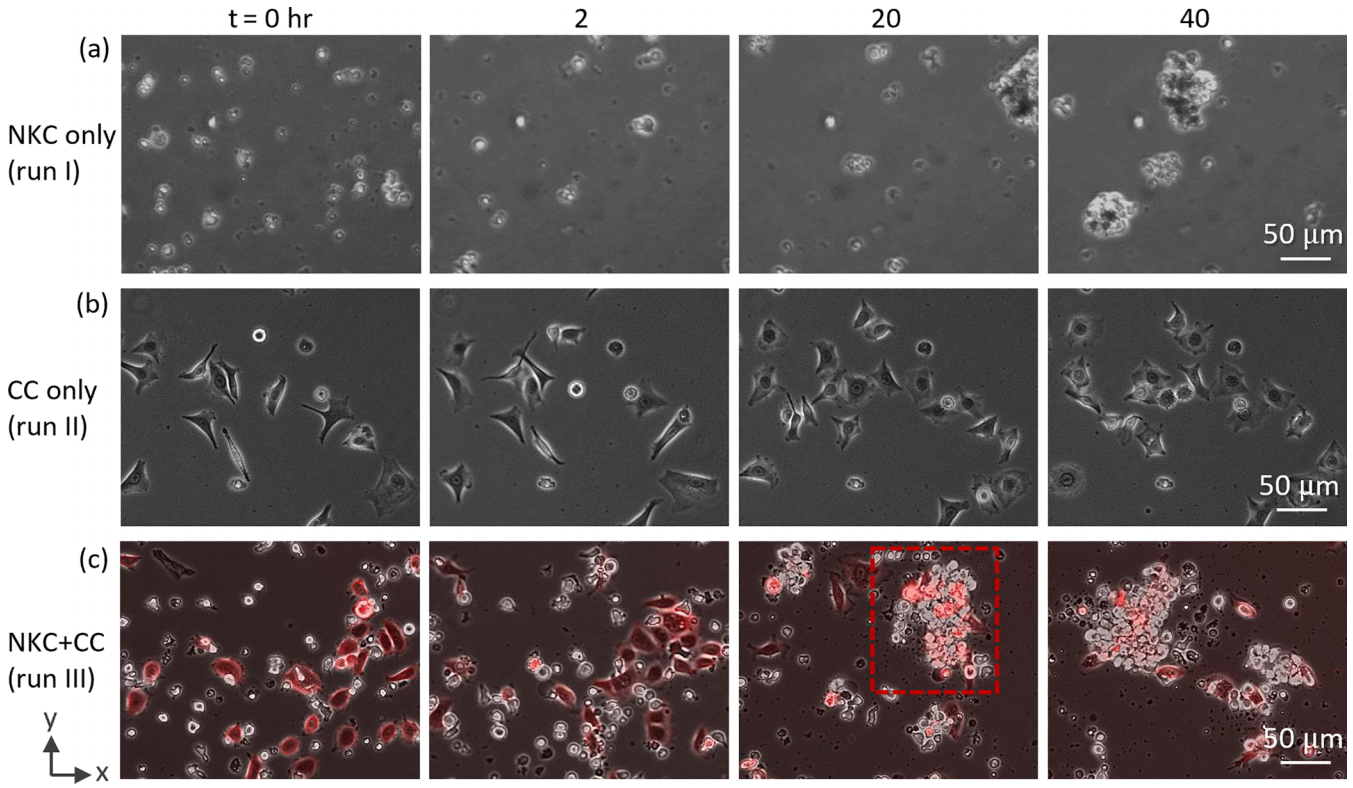

FIG. 1. Sequential microscope images of NKCs and CCs in monocultures and coculture. Sequential microscope images of cells in run I [NKC only, (a)], run II [CC only, (b)], and run III [binary mixture of NKC and CC, (c)], respectively, at different t. In those runs, NKCs are cultured at $t = 0$ and CCs are cultured at $t = -24$ hr. The small bright spots are the floating NKCs. In (c), fluorescent images in which CCs stably expressing LifeAct-RFP are marked in red and combined with NKC images to further distinguish NKCs from CCs. The dashed box marks the region enlarged in Fig. 3. These images show that as time increases, NKCs and CCs gradually aggregate into clusters in all three runs. However, the clustering behaviors differ across the three conditions.

NKC/CC mixture experiment (run III), CCs stably expressing LifeAct-RFP (5×10^4 cells/dish) are seeded in a collagen-coated dish for 24 hours, then stimulated with 10^6 NKCs. For the FC only experiment (run IV), 10^4 FCs are randomly distributed in a culture dish. For the NKC/FC mixture experiment (run V), FCs (10^4 cells/dish) were cultured for 24 hours, followed by stimulation with 10^6 NKCs. The cell positions are digitally tracked from video images obtained from phase contrast microscopy. For the convenience of visualization, CC positions are further distinguished by fluorescent microscopy. Each run is repeated three times under the same experimental control.

Figures 1(a)–1(c) show the sequential images of NKCs (run I), CCs (run II), and the binary mixture of NKC and CCs (run III), respectively, from the dilute state. The images in Figs. 1(a) and 1(b) are phase contrast images. The images in Fig. 1(c) are the overlaid images of phase contrast and fluorescent images, where CCs stably expressing LifeAct-RFP are marked in red. In Figs. 1(a) and 1(c), the time t is set to zero at the time of adding NKCs in the culture dishes (CCs are cultured at $t = -24$ hr), and the small bright spots are the floating NKCs not anchored on substrates. With increasing time, NKCs and CCs gradually aggregate into clusters in the three runs. However, the clustering behaviors are different in these three runs.

Figure 2(a) shows the spatiotemporal evolution of NKC (left) and CC (right) clusters denoted by colored patches in the xyt space of run I and run II from the same region as that of Figs. 1(a) and 1(b), respectively. In both runs, cells gradually aggregate into clusters with increasing time. Figure 2(b) shows the size distribution of NKC (left, blue dots) and CC (right, pink dots) clusters in runs I and II, respectively, evidencing the aggregation of clusters with increasing time, especially the formation of larger clusters through absorbing small clusters in the late stage. Note that CCs are cultured at $t = -24$ hr and thereby with fewer small clusters at $t = 0$.

For the binary mixture of NKC and CC (run III), Fig. 2(c) shows the spatiotemporal evolution of NKC (left) and CC (right) clusters in run III. Figure 2(d) further shows the corresponding size distributions of NKC (left) and CC (right) clusters. At $t = 0$ hr, NKCs are randomly distributed in the culture dish in which CCs are already cultured for 24 hrs. After the onset of culturing NKCs, NKCs quickly anchor to CCs and form clusters. With increasing time, they further recruit the nearby NKCs to form larger clusters than those in the NKC only case of Figs. 2(a) and 2(b) to kill CCs (see the larger NKC clusters at $t = 20$ and 40 hr from the left panel of Fig. 2(c), and Supplemental Material Video S1 [44]). Note that NKCs are usually surrounded or on top of CCs, evidenced by the almost overlapped positions of NKC and CC clusters at $t = 20$ and 40 hr in Fig. 2(c). For CCs in the initial stage, they quickly aggregate into larger clusters [e.g., the large purple cluster at $t = 20$ hr from the right panel of Fig. 2(c)] than those at the same time of the CC only run [Figs. 2(a) and

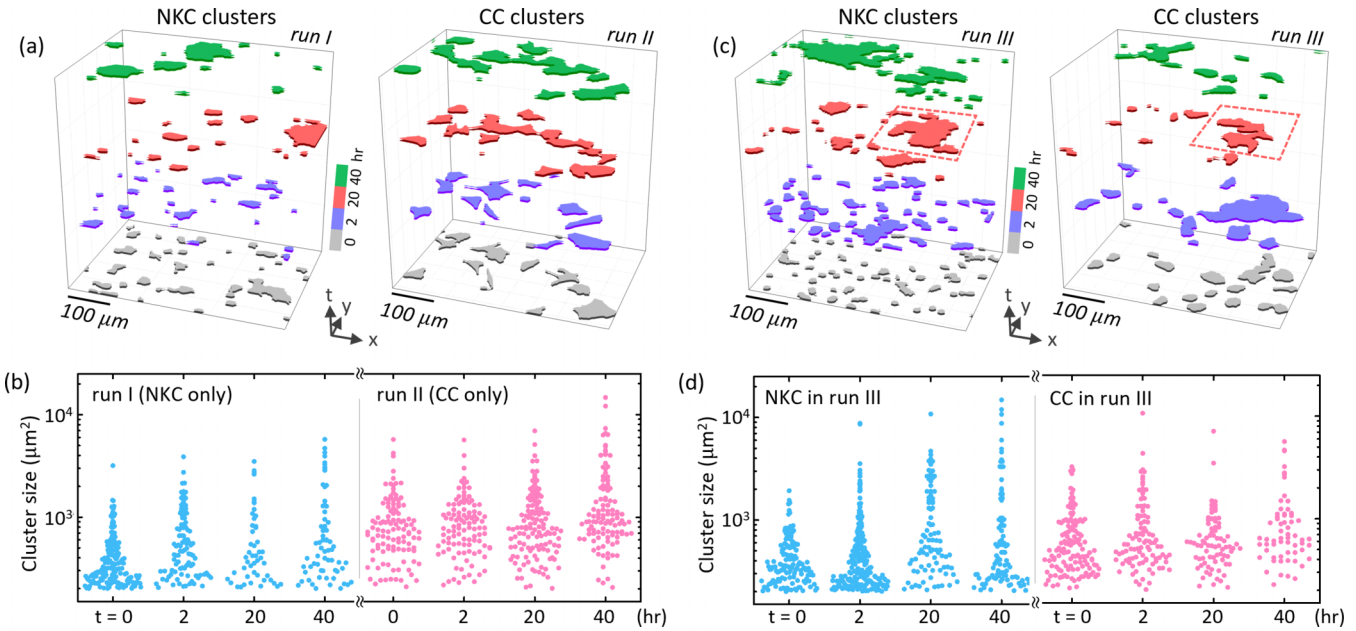

FIG. 2. Spatiotemporal evolution and size statistics of NKC and CC clusters. (a) Spatiotemporal distribution of NKC (left) and CC (right) clusters indicated by colored patches of run I and run II from the same region as that of Figs. 1(a) and 1(b), respectively. (b) NKC (left) and CC (right) cluster size distribution at different times from a $1.05 \times 1.4\,\mathrm{mm}^2$ region in run I and run II, respectively. (c) and (d) Similar plots to those of (a) and (b) for the NKC clusters and CC clusters in run III of NKC/CC binary mixture. The dots in (b) and (d) denote the size of each cluster in the field of view at the corresponding time. In (c), the dashed boxes mark the region enlarged in Fig. 3. These results are consistent with the strong coupling between NKC and CC clustering dynamics.

2(b)] to protect themselves from NKC attack. However, with further increasing time, instead of the monotonic growing CC cluster size in the CC only run, CC clusters gradually shrink through NKC killing [see smaller clusters at $t = 20$ and 40 hr from the right panel of Fig. 2(c)]. The above behaviors evidence the strong coupling between NKC and CC clustering dynamics.

Let us zoom in on a certain cluster to get more details of the dynamical interactions. Figure 3(a) shows the sequential images of a cluster enlarged from the dashed box in Figs. 1(c) and 2(c) from $t = 20$ to 22 hr (bottom to top). The images are the overlaid images of phase contrast and fluorescence images, where CCs are marked in red and the gray spots are NKCs. It shows a collective motion of both the NKC and CC clusters. However, the motion of the individual cells in the cluster is more complicated. Each purple dot in Fig. 3(a) shows a CC position which initially locates at the center of the NKC cluster at $t = 20$ hr. It moves from the center to the boundary of the NKC cluster, showing that CC tries to escape from the attack of the NKC cluster. The dashed circle in Fig. 3(a) further shows a CC that successfully escapes from the NKC cluster. However, it is accompanied by a small NKC cluster shedding, associated with the escaping CC. Namely, in addition to the aggregation and merging of the NKC clusters (see another example of NKC cluster merging in Fig. S1 of Supplemental Material [44]), NKC clusters can also dissociate from a larger NKC cluster (see another example of NKC cluster splitting in Fig. S2 of Supplemental Material [44]).

Figure 3(b) depicts some typical CC and NKC trajectories in the xyt space. The colored patches denote NKC clusters at different times. The purple and lavender curves show CC trajectories initially from the yellow dots and the dashed circles in Fig. 3(a), respectively. Note that the escaped CC (lavender curve) moves outside the field of view during $t = 21$ to 22 hr. Each pair of NKC trajectories (magenta and pink; blue and cyan) are the typical NKC trajectories whose initial positions are nearby each other. They show collective fluctuations of NKC trajectories in the NKC cluster. These back-and-forth collective motions of neighboring NKCs could be attributed to the feedback from the CC-NKC and NKC-CC interactions, which cause NKC aggregation and cluster formation around CCs. Figure 3(c) further shows the projections of the trajectories in Fig. 3(b) on the xy plane. The gray shaded region and the region encircled by the dashed lavender curve indicate the NKC and CC cluster at $t = 20$ hr. This plot reveals the escaped tendency of CCs through CC cluster splitting under NKC attack, and the collective fluctuation of NKCs in NKC clusters.

For the statistical behaviors of NKC motion, Fig. 3(d) shows the waterfall plots of probability distribution function $P_{v_{x'}}$ at different times, where $v_{x'}$ is the NKC velocity (from the velocity field obtained through particle imaging velocimetry) along the NKC mean flow direction (x' axis) in run I and run III [45,46]. NKCs in run I have a widespread initial velocity distribution whose average deviates from zero. The large nonzero average can be attributed to the large drifting motion of small NKC clusters with the background flow. With increasing t, NKC clusters with increasing sizes are formed, and the drift gradually weakens. On the other hand, NKCs in run III [bottom panel in Fig. 3(d)] only exhibit obvious drifting motion at $t = 0$ hr, which is significantly reduced after anchoring on CC clusters. The non-Gaussian tail of $P_{v_{x'}}$ in the later stage is suppressed (Fig. S4(a) of Supplemental Material shows the similar suppression of $P_{v_{y'}}$ [44]).

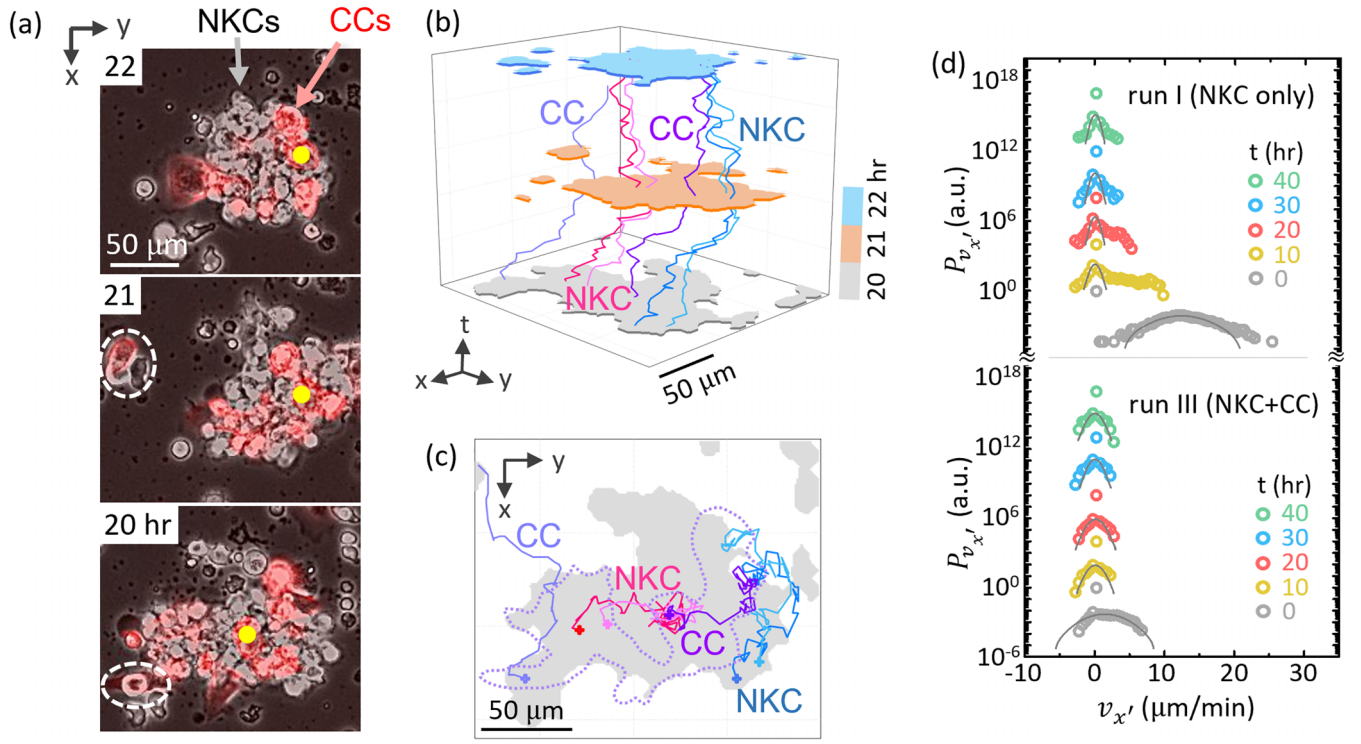

FIG. 3. Cluster dynamics and velocity statistics in NKC-CC coculture. (a) Sequential images of run III enlarged from the dashed box in Figs. 1(c) and 2(c), from $t = 20$ (bottom) to 22 (top) hr. CCs are marked in red in the overlay of phase and fluorescent images and NKCs are the bright spots. The yellow dots indicate the position of a certain CC at different t. The white dashed ellipses specify the CC that escaped from the main NKC cluster. (b) A few typical NKC (magenta, pink, blue, and cyan curves) and CC trajectories (purple and lavender curves) in the xyt space in run III. The colored patches are NKC clusters at different times. (c) Projections of the trajectories in (b) on the xy plane. The gray shaded region and the region encircled by the dashed lavender curve are the NKC and CC clusters, respectively, at $t = 20$ hr. (d) Waterfall plots of probability distribution function of $v_{x'}$, the NKC velocity along the NKC mean flow direction, at different t from a $1.05 \times 1.4\,\mathrm{mm}^2$ region, in run I (top) and run III (bottom). Gray curves correspond to the best Gaussian fits, without counting the distribution of cells whose $v_{x'} = 0$. These observations are consistent with CC escape events associated with CC cluster splitting during NKC attack, together with collective fluctuating motion of NKCs within NKC clusters.

In contrast, in run IV co-cultured with fibroblasts (normal cells), NKC exhibits very different behaviors. Figures 4(a) and 4(b) show the sequential images of the FC only run (run IV) and the binary mixture of NKC and FC (run V) at different t, respectively. In Fig. 4, the dark spindle-shaped cells are FCs, and the bright spots are NKCs. FCs remain nearly immobile in both run IV and run V, meaning that the presence of NKCs does not affect FC motion.

Figure 4(c) shows a few typical NKC trajectories (colored curves) in the xyt space in run V, from the same area as those in the boxed region of Fig. 4(b). The darker and lighter color-coded patches are the NKC and FC clusters at different times, respectively. Figure 4(d) depicts the corresponding projections of the NKC trajectories on the xy plane, where the darker and lighter gray patches are the NKC and FC clusters at $t = 20$ hr, respectively. It clearly demonstrates that, NKCs keep scouting around the entire cell body to identify whether it is a cancer cell, rather than sticking at a certain spot for attacking. It leads to the anisotropic NKC motion.

Comparing with the NKC clusters in the NKC monoculture shown in Fig. 1(a) and in the NKC-CC coculture shown in Fig. 1(c), the sizes of the NKC clusters scouting around the FC boundary are much smaller. This can also be statistically evidenced by the much shorter tails of the NKC cluster size distribution shown in Fig. 4(e) for the NKC-FC co-culture than those shown in Fig. 2(b) for the NKC monoculture and Fig. 2(d) for the NKC-CC co-culture. These observations suggest that large NKC aggregates are less frequent in NKC-FC co-culture than in NKC-CC co-culture under our assay conditions. A further nonexclusive possibility is that the presence of the FC effectively redistributes NKCs along the FC perimeter and promotes boundary-guided motion.

To quantify the alignment of NKC motion with FC geometry, we further measured the angle θ between the instantaneous NKC velocity vector and the tangent direction of the local FC boundary, as shown in Fig. 5. This local definition avoids reliance on a global reference axis and directly captures guidance by the nearby FC morphology. To suppress tracking noise and short-scale fluctuations, we analyzed only NKCs that (i) were in direct contact with the FC boundary, (ii) exhibited displacements exceeding 15 μm within $\Delta t = 30$ min (NKC diameter ~10 μm, and (iii) regions where the FC boundary underwent large deformation over Δt were excluded, since the local tangent direction would not remain well defined. The resulting θ distribution provides a statistical measure of FC-guided NKC motion. It manifests that the instantaneous velocity of the NKC is mainly tangential to the local FC boundary, as the NKC scouts around the

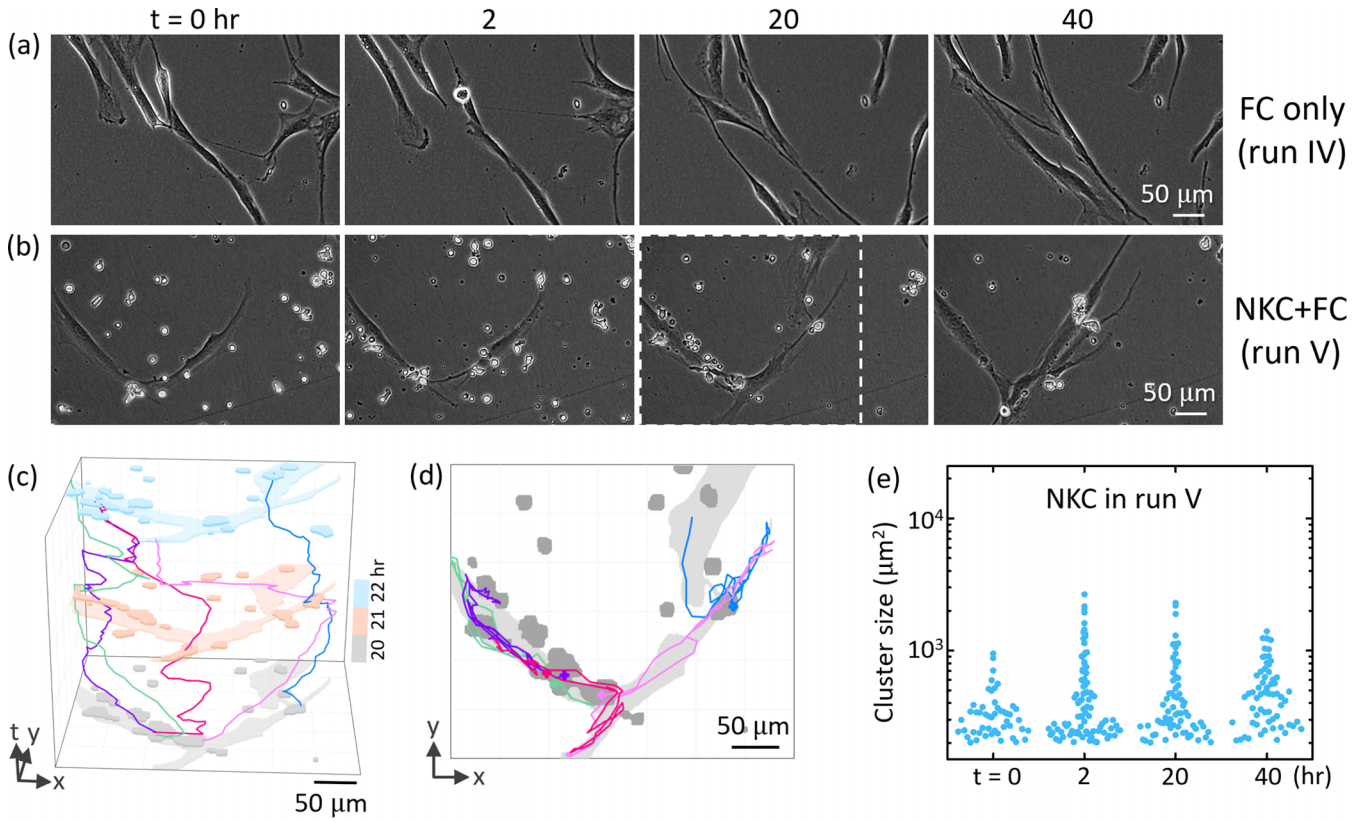

FIG. 4. NKC scouting dynamics and suppressed aggregation in NKC-FC co-culture. (a), (b) Image sequences of FCs (elongated cells) of run IV and the binary mixture of FCs and NKCs (round cells) at different t, respectively. In (b), the dashed box marks the region enlarged in (c) and (d). (c) A few typical NKC trajectories (colored curves) in the xyt space of run V, from the same area as those in the boxed region of (b). The colored patches are the NKC clusters (dark) and FCs (light) at different times. (d) Projections of the trajectories in (c) on the xy plane, with the regions occupied by NKC clusters (dark gray) and FCs (light gray) at $t = 20$ hr, respectively. (e) NKC cluster size distribution at different times from a $1.05 \times 1.4\,\mathrm{mm}^2$ region (field of view) in run V. The dots denote the size of each cluster in the field of view at the corresponding time. These results show that NKCs exhibit continuous scouting motion along the elongated FC body, consistent with anisotropic migration and suppressed NKC clustering.

FC, which can also be demonstrated in the trajectory plot of Fig. 4(d) and in Supplemental Material Video S2 [44].

In conclusion, we have investigated the spatiotemporal dynamical behaviors of natural killer cells (NKCs) encountering fibroblast/cancer cells. At the onset of the co-culturing of NKCs and CCs, floating NKCs drift and then attach to CCs. The anchored NKCs further recruit neighboring NKCs to form larger NKC clusters than those NKC clusters in the absence of CCs to facilitate the killing. The presence of CCs slows down the motion of NKCs, and makes NKCs exhibit collective fluctuating motion within dynamically reorganizing clusters around the aggregating sites, which can also drift associated with the merging or splitting of the CC clusters. After the death of CCs, NKCs move away from CCs. For CCs, they initially also form larger clusters than those of the CC only culture to protect themselves, after sensing the initial approach and attack from NKCs. The further gradual attacking of NKCs gradually decreases the CC cluster size, unlike the monotonic gradual increase of CC cluster size in the CC only case.

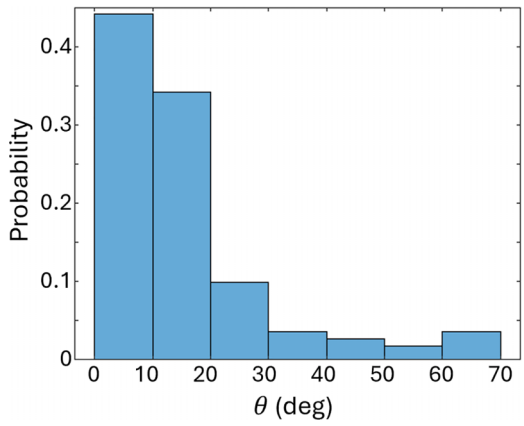

FIG. 5. Probability distribution of the angle θ between the instantaneous NKC velocity vector and the tangent direction of the local FC boundary in NKC-FC coculture.

In contrast, in the binary mixture of NKC and normal FC (run V), NKCs keep scouting the FC by moving along the main axis of the FC body, without anchoring and recruiting other NKCs for forming larger NKC clusters. Under our assay conditions, NKCs exert little influence on FC dynamics. From a dynamical perspective, NKCs in NKC-FC co-culture therefore exhibits directed motion without the pronounced clustering observed in the NKC-CC co-culture. Identifying the microscopic interactions responsible for this behavioral

switch is beyond the scope of the present work, but it provides an appealing target for future mechanistic experiments and theoretical modeling.

Within the constraints of our assay, NK-92 collectives exhibit two reproducible modes—anchoring-aggregation (forming large NKC clusters) killing near cancer cells and scouting (in the form of small NKC clusters) near fibroblasts—that differentiate the two different targets we tested. The above different dynamical responses are the important realization of this study. These dynamics provide a label-light functional signature under our specific conditions. Establishing generality will require testing additional normal cell types and tumor lines, validating with primary/autologous NKCs, and adding orthogonal cytotoxicity readouts. We therefore present this work as a quantitative framework and hypothesis generator linking mesoscale coordination to effector function, rather than a universal classifier.

This work is supported by the National Science and Technology Council of Taiwan, under Contract No. NSTC-114-2112-M-008-013.

Data availability. The data that support the findings of this article are not publicly available upon publication because it is not technically feasible and/or the cost of preparing, depositing, and hosting the data would be prohibitive within the terms of this research project. The data are available from the authors upon reasonable request.

[1] A. Cavagna, A. Cimarelli, I. Giardina, G. Parisi, R. Santagati, F. Stefanini, and M. Viale, Scale-free correlations in starling flocks, Proc. Natl. Acad. Sci. USA **107**, 11865 (2010).

[2] N. C. Makris, P. Ratilal, D. T. Symonds, S. Jagannathan, S. Lee, and R. W. Nero, Fish population and behavior revealed by instantaneous continental shelf-scale imaging, Science **311**, 660 (2006).

[3] A. Sokolov, I. S. Aranson, J. O. Kessler, and R. E. Goldstein, Concentration dependence of the collective dynamics of swimming bacteria, Phys. Rev. Lett. **98**, 158102 (2007).

[4] H. P. Zhang, A. Be'er, E.-L. Florin, and H. L. Swinney, Collective motion and density fluctuations in bacterial colonies, Proc. Natl. Acad. Sci. USA **107**, 13626 (2010).

[5] H. H. Wensink, J. Dunkel, S. Heidenreich, K. Drescher, R. E. Goldstein, H. Löwen, and J. M. Yeomans, Meso-scale turbulence in living fluids, Proc. Natl. Acad. Sci. USA **109**, 14308 (2012).

[6] C. Chen, S. Liu, X. Shi, H. Chaté, and Y. Wu, Weak synchronization and large-scale collective oscillation in dense bacterial suspensions, Nature (London) **542**, 210 (2017).

[7] A. Szabó, R. Ünnep, E. Méhes, W. O. Twal, W. S. Argraves, Y. Cao, and A. Czirók, Collective cell motion in endothelial monolayers, Phys. Biol. **7**, 046007 (2010).

[8] T. Vicsek, A. Czirók, E. Ben-Jacob, I. Cohen, and O. Shochet, Novel type of phase transition in a system of self-driven particles, Phys. Rev. Lett. **75**, 1226 (1995).

[9] T. E. Angelini, E. Hannezo, X. Trepat, M. Marquez, J. J. Fredberg, and D. A. Weitz, Glass-like dynamics of collective cell migration, Proc. Natl. Acad. Sci. USA **108**, 4714 (2011).

[10] V. Guttal and I. D. Couzin, Leadership, collective motion and the evolution of migratory strategies, Commun. Integr. Biol. **4**, 294 (2011).

[11] H. H. Wensink and H. Löwen, Emergent states in dense systems of active rods: From swarming to turbulence, J. Phys.: Condens. Matter **24**, 464130 (2012).

[12] A. Puliafito, L. Hufnagel, P. Neveu, S. Streichan, A. Sigal, D. K. Fygenson, and B. I. Shraiman, Collective and single cell behavior in epithelial contact inhibition, Proc. Natl. Acad. Sci. USA **109**, 739 (2012).

[13] M. L. Wynn, P. Rupp, P. A. Trainor, S. Schnell, and P. M. Kulesa, Follow-the-leader cell migration requires biased cell–cell contact and local microenvironmental signals, Phys. Biol. **10**, 035003 (2013).

[14] A. Czirók, K. Varga, E. Méhes, and A. Szabó, Collective cell streams in epithelial monolayers depend on cell adhesion, New J. Phys. **15**, 075006 (2013).

[15] B. Li and S. X. Sun, Coherent motions in confluent cell monolayer sheets, Biophys. J. **107**, 1532 (2014).

[16] Y.-S. Su, H.-C. Wang, and L. I, Suppressing turbulence of self-propelling rods by strongly coupled passive particles, Phys. Rev. E **91**, 030302(R) (2015).

[17] D. Bi, J. H. Lopez, J. M. Schwarz, and M. L. Manning, A density-independent rigidity transition in biological tissues, Nat. Phys. **11**, 1074 (2015).

[18] S. Garcia, E. Hannezo, J. Elgeti, J.-F. Joanny, P. Silberzan, and N. S. Gov, Physics of active jamming during collective cellular motion in a monolayer, Proc. Natl. Acad. Sci. USA **112**, 15314 (2015).

[19] J.-A. Park *et al.*, Unjamming and cell shape in the asthmatic airway epithelium, Nat. Mater. **14**, 1040 (2015).

[20] G. Duclos, C. Erlenkämper, J.-F. Joanny, and P. Silberzan, Topological defects in confined populations of spindle-shaped cells, Nat. Phys. **13**, 58 (2017).

[21] C.-Y. Liu, H.-Y. Chen, and L. I, Scale-free aggregation and interface fluctuations of cancer clusters in cancer-endothelial cell mixtures: From the dilute state to confluent monolayer, Phys. Rev. Res. **3**, L032050 (2021).

[22] C.-Y. Liu, Y.-X. Zhang, and L. I, Two-stage structural and slowing-down percolation transitions in the densifying cancer cell monolayer, Phys. Rev. Lett. **129**, 148102 (2022).

[23] P. Friedl and D. Gilmour, Collective cell migration in morphogenesis, regeneration and cancer, Nat. Rev. Mol. Cell Biol. **10**, 445 (2009).

[24] E. Anon, X. Serra-Picamal, P. Hersen, N. C. Gauthier, M. P. Sheetz, X. Trepat, and B. Ladoux, Cell crawling mediates collective cell migration to close undamaged epithelial gaps, Proc. Natl. Acad. Sci. USA **109**, 10891 (2012).

[25] K. D. Nnetu, M. Knorr, D. Strehle, M. Zink, and J. A. Käs, Directed persistent motion maintains sheet integrity during multi-cellular spreading and migration, Soft Matter **8**, 6913 (2012).

[26] O. Ilina and P. Friedl, Mechanisms of collective cell migration at a glance, J. Cell Sci. **122**, 3203 (2009).

[27] D. T. Tambe *et al.*, Collective cell guidance by cooperative intercellular forces, Nat. Mater. **10**, 469 (2011).
[28] A. Haeger, M. Krause, K. Wolf, and P. Friedl, Cell jamming: Collective invasion of mesenchymal tumor cells imposed by tissue confinement, Biochim. Biophys. Acta **1840**, 2386 (2014).
[29] A. Labernadie *et al.*, A mechanically active heterotypic E-cadherin/N-cadherin adhesion enables fibroblasts to drive cancer cell invasion, Nat. Cell Biol. **19**, 224 (2017).
[30] A. J. Kabla, Collective cell migration: Leadership, invasion and segregation, J. R. Soc. Interface **9**, 3268 (2012).
[31] W. K. Chang, C. Carmona-Fontaine, and J. B. Xavier, Tumour–stromal interactions generate emergent persistence in collective cancer cell migration, Interface Focus. **3**, 20130017 (2013).
[32] C. P. Beatrici, R. M. C. de Almeida, and L. G. Brunnet, Mean-cluster approach indicates cell sorting time scales are determined by collective dynamics, Phys. Rev. E **95**, 032402 (2017).
[33] H.-Y. Chen, Y.-T. Hsiao, S.-C. Liu, T. Hsu, W.-Y. Woon, and L. I, Enhancing cancer cell collective motion and speeding up confluent endothelial dynamics through cancer cell invasion and aggregation, Phys. Rev. Lett. **121**, 018101 (2018).
[34] R. B. Herberman, H. T. Holden, C. C. Ting, D. L. Lavrin, and H. Kirchner, Cell-mediated immunity to leukemia virus- and tumor-associated antigens in mice, Cancer Res. **36**, 615 (1976).
[35] E. Vivier, D. H. Raulet, A. Moretta, M. A. Caligiuri, L. Zitvogel, L. L. Lanier, W. M. Yokoyama, and S. Ugolini, Innate or adaptive immunity? The example of natural killer cells, Science **331**, 44 (2011).
[36] E. Vivier, S. Ugolini, D. Blaise, C. Chabannon, and L. Brossay, Targeting natural killer cells and natural killer T cells in cancer, Nat. Rev. Immunol. **12**, 239 (2012).
[37] M. Luetke-Eversloh *et al.*, NK cells gain higher IFN-γ competence during terminal differentiation, Eur. J. Immunol. **44**, 2074 (2014).
[38] L. Chiossone, P.-Y. Dumas, M. Vienne, and E. Vivier, Natural killer cells and other innate lymphoid cells in cancer, Nat. Rev. Immunol. **18**, 671 (2018).
[39] C. Guillerey, N. D. Huntington, and M. J. Smyth, Targeting natural killer cells in cancer immunotherapy, Nat. Immunol. **17**, 1025 (2016).
[40] S.-Y. Wu, T. Fu, Y.-Z. Jiang, and Z.-M. Shao, Natural killer cells in cancer biology and therapy, Mol. Cancer **19**, 120 (2020).
[41] S. Bauer, V. Groh, J. Wu, A. Steinle, J. H. Phillips, L. L. Lanier, and T. Spies, Activation of NK cells and T cells by NKG2D, a receptor for stress-inducible MICA, Science **285**, 727 (1999).
[42] P. J. Amin and B. S. Shankar, Sulforaphane induces ROS mediated induction of NKG2D ligands in human cancer cell lines and enhances susceptibility to NK cell mediated lysis, Life Sci. **126**, 19 (2015).
[43] C.-W. Hsu, J.-S. Yu, P.-H. Peng, S.-C. Liu, Y.-S. Chang, K.-P. Chang, and C.-C. Wu, Secretome profiling of primary cells reveals that THBS2 is a salivary biomarker of oral cavity squamous cell carcinoma, J. Proteome Res. **13**, 4796 (2014).
[44] See Supplemental Material http://link.aps.org/supplemental/10.1103/mf3s-pcwt for more detailed information about cell culture processes and typical NKC dynamical behaviors.
[45] W. Thielicke and E. J. Stamhuis, PIVlab–Towards user-friendly, affordable and accurate digital particle image velocimetry in MATLAB, J. Open Res. Software **2**, e30 (2014).
[46] W. Thielicke and R. Sonntag, Particle image velocimetry for MATLAB: Accuracy and enhanced algorithms in PIVlab, J. Open Res. Software **9**, 12 (2021).